





RESEARCH ARTICLE | DECEMBER 06 2022

Turbulent combustion statistics in a diffusion flame for space propulsion applications

Daniel Martinez-Sanchis  ; Andrej Sternin ; Oskar Haidn; Martin Tajmar 



Physics of Fluids 34, 125115 (2022)

<https://doi.org/10.1063/5.0130537>



Physics of Fluids
Special Topic: Overview of Fundamental and Applied Research in Fluid Dynamics in UK
[Submit Today](#)



Turbulent combustion statistics in a diffusion flame for space propulsion applications

Cite as: Phys. Fluids **34**, 125115 (2022); doi: [10.1063/5.0130537](https://doi.org/10.1063/5.0130537)

Submitted: 12 October 2022 · Accepted: 14 November 2022 ·

Published Online: 6 December 2022



View Online



Export Citation



CrossMark

Daniel Martinez-Sanchis,^{1,a)}  Andrej Sternin,^{1,2}  Oskar Haidn,¹ and Martin Tajmar² 

AFFILIATIONS

¹Chair of Space Propulsion, Technische Universität München, Boltzmannstraße 15, Garching, Germany

²Chair of Space Systems, Technische Universität Dresden, Marschnerstraße 32, Dresden, Germany

^{a)}Author to whom correspondence should be addressed: daniel.martinez@tum.de

ABSTRACT

The usage of direct numerical simulations for research of turbulent combustion for space propulsion applications is explored. With this goal in mind, the combustion near the injection of a fuel-rich methane–oxygen flame at 20 bar is simulated using a massively parallelized solver. The statistical properties of the relevant physical fields are examined to study interactions between turbulence and combustion. This analysis is complemented by an investigation and quantification of the error sources in direct numerical simulations of turbulent diffusion flame. A method to estimate the statistical error is derived based on the classical inference theory. In addition, critical resolution criteria are discussed using a mesh sensitivity analysis.

© 2022 Author(s). All article content, except where otherwise noted, is licensed under a Creative Commons Attribution (CC BY) license (<http://creativecommons.org/licenses/by/4.0/>). <https://doi.org/10.1063/5.0130537>

I. INTRODUCTION

Methane is a promising propellant for the next generation of space propulsion systems. It is among the most viable replacements for hydrazine,^{1–4} and it presents the potential for use in planetary ascent/descent applications.⁵ Consequently, a great effort has been invested in its research during the last decades. However, essential questions concerning mixing, ignition, and stable combustion must be addressed during the design and development process of methane-fueled engines.^{6,7} These tasks strongly rely on Computational Fluid Dynamics (CFD) software. Due to their low cost, Reynolds-averaged Navier–Stokes (RANS) solvers constitute the most extended simulation method to this date. Despite this advantage, RANS models present several shortcomings. The conditions in the combustion chamber of rocket engines deviate substantially from the standard environment for which most RANS models were devised. At high pressure, the flame front becomes thinner, and almost any relevant quantity can vary orders of magnitude within a few micrometers. The fast chemical reactions lead to high Damköhler numbers, which enable exotic phenomena, such as flame-generated turbulence.^{8–11} Due to these extreme conditions, the Turbulence–Chemistry Interactions (TCI) must be modeled. In addition, the complex turbulent dynamics are oversimplified to one or two parameters, usually the turbulent kinetic energy (TKE) k and its dissipation rate $\tilde{\epsilon}$. This reduction entails the loss of relevant physical information. Due to this limitation, detailed physical

processes cannot be captured, and TCI modeling is hindered. Reversed energy transfer, sporadic extinctions, combustion instabilities, and anisotropy are additional examples of phenomena that cannot be captured with the conventional RANS solvers but have been observed experimentally and in higher fidelity simulations. The design and development of rocket combustors are conditioned by the limited understanding of these complex processes. More detailed knowledge of the TCI is necessary to develop efficient combustion systems.^{12–14}

With increasing computational resources, scale-resolving methods, such as Large Eddy Simulations (LES) and Direct Numerical Simulations (DNS), are becoming feasible alternatives in certain contexts.^{15–19} Despite their higher fidelity, the usage of these methods is hindered by limited experience and their inherent challenges. The most obvious shortcoming of these approaches is their high computational cost, which often limits the extent of the simulation domain. Hence, it is usually necessary to restrict the analysis to certain regions since a simulation of the entire system is not always affordable. This sort of strategy demands the generation of appropriate boundary conditions. Moreover, the resolution requirements pose a relevant unknown as well. In the context of premixed flames, it is generally considered that the flame front should be resolved with 10–20 cells.^{20,21} This definition finds challenging applicability in the context of diffusion flames, where the flame thickness greatly varies over time and space. In addition to the unknown surrounding resolution

requirements, mesh sensitivity analyses are unaffordable for most cases. In scale-resolving simulations, the computational cost scales with the fourth or fifth power of the resolution. Since the sheer compliance with basic resolution requirements brings most systems to their capability limits, slight resolution improvements become prohibitive. All these challenges contrast with the simplicity of RANS. In RANS solvers, the solution error is known, and mesh sensitivity analyses are affordable in most cases since the computational cost grows with the second or third power of the resolution. All the mentioned issues hinder the applicability of DNS and LES for many industry-relevant problems. These simulations have the potential to overcome the limitations of the conventional RANS solvers, shedding light on the complex fluid dynamics that occur in combustion chambers for rocket engines. Future design programs can benefit from scale-resolving simulations if their uncertainties, computational costs, and requirements are better understood. Hence, research concerning their usage is necessary to widen the applicability window. This paper addresses the application of DNS for combustion chambers of liquid rocket engines. A turbulent diffusion flame is simulated using high fidelity EBI–DNS solver. The simulation results are examined to pinpoint the valuable information that can be retrieved. Furthermore, the simulation was repeated using different resolutions to perform a mesh sensitivity analysis and evaluate numerical uncertainties. The main goal of the current work is to demonstrate the capabilities of DNS for space propulsion applications.

The rest of the paper is structured as follows: In Sec. II, the main concepts necessary for analyzing the statistics of a turbulent combust-ing flow are provided. In Sec. III, the simulation framework is detailed. The main physical processes are discussed in Sec. IV. The uncertainty surrounding the numerical simulations is examined in Sec. V. Finally, the results are summarized in Sec. VI.

II. THEORETICAL BACKGROUND

This section is devoted to introducing the basic concepts for tur-bulent combustion, which will be extensively used during the discus-sion of the results. The text is structured in two subsections. First, basic notions for the statistical characterization of turbulent flows are introduced. The Subsection II B addresses the core concepts related to diffusion flames.

A. Turbulence

Due to the chaotic nature of turbulence,^{22,23} a stochastic approach is deemed suitable as opposed to the deterministic one. The most relevant statistical parameter of a general physical quantity q is the Reynolds average (i.e., time average) $\bar{q} = (1/t_{\text{end}}) \int_0^{t_{\text{end}}} q(t) dt$. In flows with significant variations in specific volume, it is convenient to weigh the observed values with density. This is the basis for the Favre-average,²⁴ expressed as follows:

$$\bar{q} = \frac{1}{\bar{\rho} t_{\text{end}}} \int_0^{t_{\text{end}}} \rho(t) q(t) dt. \quad (1)$$

This value is used to define Favre fluctuations $q''(t)$ as the observed deviation from the expected value, i.e., $q''(t) = q(t) - \bar{q}$. Fluctuations around the average are a fundamental aspect of turbulent flows. Therefore, it is necessary to quantify them. Since the averaged fluctua-tions equal zero, i.e., $\bar{q}'' = 0$, we resort to higher-order statistics.

The most common indicator is the second-order moment, i.e., $\bar{\sigma}_q^2 = q''^2$, which is referred to as the variance.

In experiments and unsteady simulations, it is not possible to average a property over an infinite time. Therefore, the following approximated average value \bar{q}^* is instead obtained:

$$\bar{q}^* = \frac{\sum_{i=1}^n q(t_i) \rho(t_i)}{\sum_{i=1}^n \rho(t_i)} = \bar{q} + \bar{q}^e, \quad (2)$$

where \bar{q}^e denotes the error due to insufficient recorded observations of q used for averaging. Assuming that the error follows a Gaussian dis-tribution, using n independent measurements, it is possible to estimate the probability that it surpasses a given threshold value as²⁵

$$P\left(\bar{q}^e > \frac{\bar{\sigma}_q^*}{\sqrt{n}} t(\alpha, n)\right) = \alpha, \quad (3)$$

where $\bar{\sigma}_q^*$ is the measured standard deviation of \bar{q} , α is the significance level, and t is the t -value. The confidence level $CI = 1 - \alpha$ indicates the likeliness of the error to staying below the given threshold, and it is usually taken as 95%, corresponding to $\alpha = 0.05$. It is important to remark that the expression in (3) uses Favre-averaged quantities, which deviates from the classical formulation.

In turbulent flows, the most relevant fluctuations correspond to the velocity field. These are mainly characterized by their variance, which is used to define the turbulent kinetic energy (TKE) in each direction i ,

$$\tilde{k}_i = \frac{1}{2} \bar{\sigma}_{u_i}^2 = \frac{\overline{\rho u_i' u_i''}}{2\bar{\rho}}. \quad (4)$$

In combustion chambers, the turbulent kinetic energy \tilde{k} is a relevant parameter *per se* as it is related to friction losses and determines the mixing capabilities of the reactants enabling a higher burning rate compared to the laminar case.^{20,26,27} However, the more relevant aspect of this statistic is its coupling with the average velocity \tilde{u}_\odot which is manifested in the Reynolds-averaged momentum conserva-tion equation. Most RANS solvers assume isotropy in (4), i.e., $\tilde{k}_1 = \tilde{k}_2 = \tilde{k}_3$, thereby neglecting important flow features. Although this assumption might be justified in certain flows, this is not the case for turbulent flames, which are strongly anisotropic, exhibiting most of the total turbulent kinetic energy in the main flow propagation direction.^{28,29} Walls and injection posts are other regions where the turbulent flow presents a highly anisotropic behavior. Determining the spatial-temporal evolution of the turbulent kinetic energy is a core problem in turbulent flows. This development is governed by the tur-bulent kinetic energy transport equation, which originates from the Navier–Stokes conservation equations. For the case of Favre-averaged turbulent kinetic energy, it can be expressed as follows:^{30–32}

$$\begin{aligned} \frac{\partial \bar{\rho} \tilde{k}}{\partial t} + \frac{\partial \bar{\rho} \tilde{u}_j \tilde{k}}{\partial x_j} = & \underbrace{-\overline{\rho u_i' u_j''}}_{T_1} \frac{\partial \tilde{u}_i}{\partial x_j} - \underbrace{\overline{u_i''}}_{T_2} \frac{\partial \bar{p}}{\partial x_j} + \underbrace{\overline{p' u_i''}}_{T_3} + \underbrace{\overline{u_i'' \frac{\partial \tau_{ij}}{\partial x_j}}}_{T_4} \\ & - \underbrace{\frac{\partial \overline{p' u_i''}}{\partial x_i}}_{T_5} - \underbrace{\frac{\partial}{\partial x_j} \left(\frac{1}{2} \overline{\rho u_i' u_k'' u_k''} \right)}_{T_6}. \end{aligned} \quad (5)$$

The main challenge involving this equation is that the majority of the terms are unclosed. Therefore, it is necessary to develop models for their prediction. The physical meaning of these terms is discussed in the text below.

The term T_1 represents the turbulent production through mean velocity gradients. In combustion applications, this term typically presents negative values in regions far away from the walls due to the positive velocity gradients in the main flame propagation direction.

The term T_2 represents the turbulence generation through mean pressure gradients. This term was identified as one of the primary sources of flame-generated turbulence in premixed combustion for high Damköhler numbers.^{30,31} The generation of the turbulent kinetic energy is enabled by the decoupling between the Reynolds and Favre velocity fluctuations, which yield a positive time average of the Favre velocity fluctuations, i.e., $\overline{u_i''} > 0$. This term was successfully modeled by Nishiki *et al.*³¹ in the frame of premixed flames.

The terms T_3 and T_5 revolve around the coupling between pressure and velocity fluctuations. Both terms can be merged to approach them in a more compact formulation

$$T_{35} = T_3 + T_5 = -\overline{u_k'' \frac{\partial p'}{\partial x_k}}. \quad (6)$$

This term is one of the main turbulence sources in premixed turbulent flames.^{30–33} The modeling of this element for combustion applications has been approached in a previous research^{30,34,35} with limited success. Despite its relevance, it is often neglected in commercial solvers.³⁶

The behavior of the term T_6 strongly depends on the combustion regime. In statistically planar premixed flames, T_6 acts mainly as a turbulence source, especially if the Damköhler number is small. In shear layers, this term is strongly dominated by the stratification of TKE, and it may present negative or positive values depending on whether the TKE profile through the reactive shear layer follows convex or concave trends.³⁷

The term T_4 describes molecular diffusion and viscous dissipation. It is possible to recast this term as follows:

$$T_4 = -\overline{\rho \tilde{\epsilon}} + \underbrace{\left(\overline{u_i'' \frac{\partial}{\partial x_k} \left(\mu \frac{\partial u_k}{\partial x_i} \right)} - \frac{2}{3} \overline{u_i'' \frac{\partial}{\partial x_j} \left(\mu \frac{\partial u_k}{\partial x_k} \right)} \right)}_{T_v} + \frac{\partial}{\partial x_j} \left(\mu \frac{\partial \tilde{k}}{\partial x_j} \right), \quad (7)$$

where $\tilde{\epsilon}$ is the Favre-averaged dissipation rate. In statistically planar flames, the approximation $T_4 \approx -\overline{\rho \tilde{\epsilon}}$ holds quite accurately since dissipation dominates the other two terms in (7). For diffusion flames, in their shear layers, the viscous molecular transport, i.e., $\nabla \cdot (\mu \nabla \tilde{k})$, can present a substantial contribution. Nevertheless, this term poses no challenge in terms of predictability since it is closed.

The dissipation rate of the turbulent kinetic energy requires further discussion. The relevance of this parameter extends beyond its role in the TKE transport equation, and it is commonly used to characterize and describe turbulent flows. The dissipation rate accounts for the natural decay of turbulence due to viscosity, and it is defined as follows:

$$\tilde{\epsilon} = \mu \left(\frac{\partial u_i''}{\partial x_j} \frac{\partial u_i''}{\partial x_j} \right) / \overline{\rho}. \quad (8)$$

In flow locations far away from the walls and in the absence of velocity and density gradients, the time derivative of the turbulent kinetic energy can be expressed as follows:

$$\frac{\partial \tilde{k}}{\partial t} = -\tilde{\epsilon}. \quad (9)$$

Linearizing this rate of turbulent kinetic energy “loss,” it is possible to obtain a rough assessment of the vortexes lifetime

$$t_T = \tilde{k} / \tilde{\epsilon}. \quad (10)$$

Turbulence arises from the superposition of a wide number of eddies that span over various length scales. Each eddy size presents a characteristic timescale. These turbulent scales are essential for researching TCI since their overlap with their chemical counterparts determines how turbulent and combustion processes influence one another.³⁸ Therefore, it is necessary to establish definitions for the most characteristic scales. The size of the largest eddies can be estimated as follows:³⁹

$$\tilde{L} = \sqrt{\tilde{k}^3 / \tilde{\epsilon}}. \quad (11)$$

On the other extreme, we find the smallest vortical structures, which are referred to as the Kolmogorov eddies. Their length can be estimated as a function of the viscosity and the dissipation rate

$$\tilde{\eta} = \left(\frac{(\tilde{\mu} / \overline{\rho})^3}{\tilde{\epsilon}} \right)^{1/4} = \left(\frac{\tilde{\nu}^3}{\tilde{\epsilon}} \right)^{1/4}. \quad (12)$$

In addition to their physical relevance, the size of the smallest eddies is a crucial aspect from a computational standpoint as it determines the necessary grid size in DNS. The criterion $\Delta x_{\max} \approx 2.1\eta$ established by Yeung and Pope^{40,41} is often taken as a reference. If a larger cell size is used, models to account for the sub-grid turbulent properties are required to account for the non-resolved eddies.

The degree of turbulence is often described using the Reynolds number, representing the ratio between the destabilizing (i.e., inertial) and dampening effects. For the largest eddies, the turbulent Reynolds number can be defined as follows:

$$Re_L = \frac{\tilde{k}^2}{\tilde{\epsilon} \nu}. \quad (13)$$

This parameter is useful to define the local intensity of the flow’s turbulent behavior. A global definition can be stated to describe the overall turbulent nature of a fluid system. For channel flows, the definition of a global Reynolds number is conventionally stated as follows:

$$Re = \frac{U \phi_H}{\nu}, \quad (14)$$

where U is the freestream flow velocity, and ϕ_H is the hydraulic diameter.

B. Non-premixed combustion

In diffusion flames, combustion progress is limited to the local mixing of the fuel and the oxidizer. These processes evolve simultaneously, and their development is crucial for the performance of any combustion device. This section introduces the basic turbulent

quantities that describe the turbulent mixing and the combustion progress, i.e., the mixture fraction Z and the progress variable c in the frame of non-premixed combustion.

The mixture fraction represents the local fraction of hydrocarbon content. For a chemical species made up of n_C , n_H , and n_O carbon, hydrogen, and oxygen atoms, it can be expressed as follows:

$$Z_i = \frac{A_C n_C + A_H n_H}{A_C n_C + A_H n_H + A_O n_O} \approx \frac{12n_C + n_H}{12n_C + n_H + 16n_O}, \quad (15)$$

where A_C , A_H , and A_O stand for the atomic weights of carbon, hydrogen, and oxygen, respectively. The individual mixture fractions can be combined to obtain the total value

$$Z = \sum_{i=1}^n Y_i Z_i, \quad (16)$$

where \textcircled{C} is the mass fraction of the i -th chemical species. This parameter indicates the local mixing of the fuel and the oxidizer. The mixture fraction definition is chosen so that it tends to zero near oxidizer injection and to unity close to the fuel-rich side. This concept is tightly coupled with the oxidizer-to-fuel ratio O/F . Indeed, it is possible to relate both parameters as: $Z = 1/(1 + O/F)$. Hence, for methane-oxygen combustion, with stoichiometric $(O/F)_{st} \approx 4$, the stoichiometric mixture fraction corresponds to $Z_{st} \approx 0.2$. In diffusion flames, most of the heat release occurs at the positions where the average mixture fraction is close to the stoichiometric value, i.e., $\bar{Z} \approx Z_{st}$.

The progress variable c ranges from zero to unity, representing the degree of completion of the combustion process. This parameter is commonly defined with expressions of the following sort:⁴²

$$c = \frac{q - q_R}{q_P - q_R}, \quad (17)$$

where q is a physical quantity associated with combustion development. In this expression, the subindexes R and P stand for reactants and products, respectively. The chosen quantity q shall present a monotonic trend to avoid ambiguity in the results.⁴³ In premixed flames, temperature, species concentration, or density are typically chosen to define the progress variable. However, the diffusion flames require more complex approaches. This is motivated by the local differences in mixing, which lead to variations in the equilibrium state to which the local mixture converges. Furthermore, the introduction of the complex chemical schemes can suppress the monotonic trends of specific quantities⁴³ and/or their linearity.⁴⁴ To circumvent these challenges, Bray *et al.*⁴⁵ proposed the following generalization of the expression in (17):

$$c = \frac{Y_c}{Y_c^{Eq}(Z)}, \quad (18)$$

where Y_c denotes the reaction progress variable,^{46,47} and $Y_c^{Eq}(Z)$ denotes the equilibrium value for a given mixture fraction. For oxygen-methane combustion at high pressures, the following expression for the reaction progress variable has been used in recent works:³⁷

$$Y_c = \frac{Y_{CO_2}}{M_{CO_2}} + \frac{Y_{CO}}{M_{CO}} + \frac{Y_{H_2O}}{M_{H_2O}} + \frac{Y_O}{M_O} + \frac{Y_H}{M_H} + \frac{Y_{OH}}{M_{OH}}. \quad (19)$$

This definition is based on the expression originally proposed by Pierce and Moin,⁴⁸ which has been used in recent studies⁴⁹ with

similar setups as the current paper. Some modifications have been implemented to account for the specific phenomena occurring in rocket propulsion, such as ionization⁵⁰ and the non-monotonic behavior of hydroxyl and hydrogen molecules.⁵¹

III. SIMULATION SETUP

In this section, the performed simulations are described along with the post-processing strategy and the resolution requirements. The text is structured in two parts. First, the overall simulation strategy is detailed, along with numerical insight concerning the used solver and the chemical mechanism. In Subsection III A, the followed post-processing methodology is briefly discussed, and the degree of accomplishment of the resolution requirements is commented.

A. Simulation strategy

The simulation framework involves two serially connected simulations. A precursor simulation computes the flow field through the injector's manifolds to obtain realistic inlet boundary conditions for the combustion chamber. These fields are subsequently fed into the main simulation, which is where mixing and combustion take place. Both simulations use periodic boundary conditions in the directions perpendicular to injection (i.e., X and Y). Directions X and Z are referred to as radial and axial, respectively. This terminology was adopted to simplify the discussion and ease analogies with coaxial injectors. However, it is important to remark that this naming is not strictly accurate since the simulated domain is not tubular but prismatic. The overall strategy and domain are displayed in Fig. 1 and detailed in the text below.

In the precursor simulation, periodic synthetic turbulence is generated at the inlet, with the scheme described in a previous work.⁵² This method is based on the research of Shur *et al.*,⁵³ which originates from the original formulation suggested by Kraichnan.⁵⁴ The main idea of these methods is the superposition of several harmonics derived from a reference turbulent kinetic energy spectrum. The development of the Synthetic Generated Turbulence (STG) into a mature turbulent flow can be validated by examining the classical statistics of turbulent flows as detailed in a previous study.⁵² Geometry and initial turbulent flow properties were based on RANS simulations of a scale methane rocket combustor discussed elsewhere.⁵⁵ However, due to the high computational cost, dimensions, and inlet velocity, \textcircled{C}_i were downscaled. As a consequence of these changes, the global Reynolds number $Re = U\phi_H/\nu$ in the injection manifolds is roughly 20 times smaller than the reference system. Despite these variations, the performed simulations remain close enough to the actual setup to enable valuable comparisons. A summary of the turbulent characteristics at injection is provided in Table I. Identical injection velocity and hydraulic diameter were chosen for both propellants. This configuration differs from the standard setups. The reason is that the resulting database will be used to investigate the interactions between chemistry and turbulence. For this reason, using identical injection characteristics is desirable since it facilitates the observation of the turbulence dynamics.

The main simulation aims to recreate the mixing and combustion nearby the injection region and far away from the combustion chamber walls. A stationary diffusion flame is simulated in a prismatic domain with dimensions $0.3 \times 0.2 \times 3$ mm and resolved with $288 \times 192 \times 2880$ cubic cells in the highest resolution simulation.

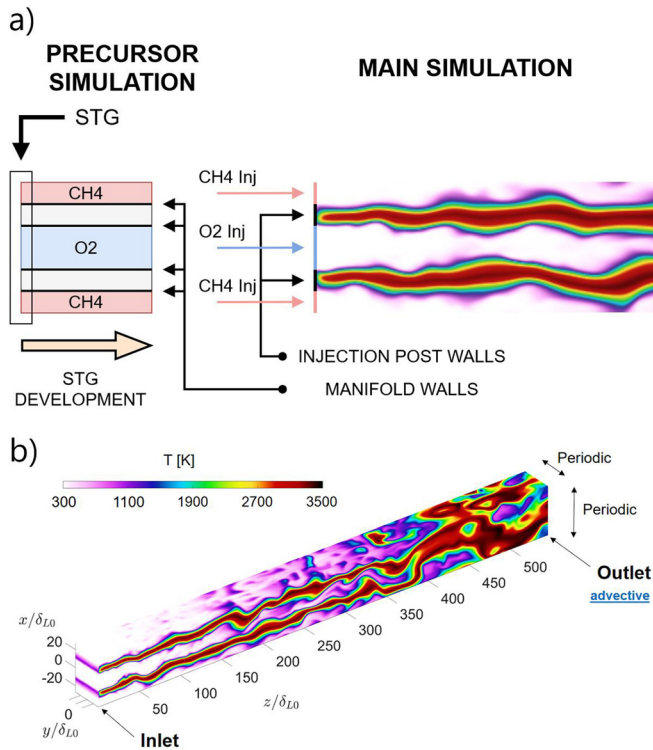


FIG. 1. General simulation strategy: Simulation sequence from the precursor to main simulation (a) schematic of the main simulation domain and boundary conditions (b).

Propellants are injected using a splitter plate configuration with an injection post wall separating oxidizer and fuel injection. The domain’s aspect ratio is 12.5, allowing for the burning of a large fraction of the injected reactants. The physical flow fields in the main simulation are resolved using the reactive solver EBI-DNS.^{56–59} This solver was developed by the Engler–Bunte Institute (EBI) for combustion technology of the Karlsruhe Institute of Technology (KIT), and it is embedded in the open-source software OpenFOAM.^{60,61} EBI-DNS solves the unsteady compressible Navier–Stokes conservation

TABLE I. Relevant turbulent scales and characteristics at injection. The parameters that vary in space are averaged over the cross section. Values are normalized with the laminar flame characteristics at stoichiometric conditions, i.e., δ_{L0} and s_{L0} , which can be consulted in Table II.

	Fuel injection	Oxidizer injection
η/δ_{L0}	0.152	0.1409
L/δ_{L0}	11.00	11.26
u_{rms}/s_{L0}	1.363	1.38
ϕ_H/δ_{L0}	24.22	24.22
U_i/s_{L0}	9.7144	9.7144
Re	3873	4274
Re_L	301.16	344.31

TABLE II. Main combustion parameters of the simulated flame.

P	Injection pressure	20 bar
T_u	Temperature of the unburnt reactants	300 K
ϕ	Global equivalence ratio	0.5
δ_{L0}	Laminar flame thickness at stoichiometric conditions	5.505 μm
s_{L0}	Laminar flame speed at stoichiometric conditions	2.5735 m/s
\tilde{c}_{end}	Average progress variable near the outlet (SC)	0.71

equations besides energy and species conservation equations using the Finite Volume Method (FVM).^{62,63} This software has been applied and validated in several combustion-related problems during the last few years.^{64–68} Massive parallelization with marginal losses in computational efficiency is feasible. Indeed, within this work, the highest resolution simulation was computed in several batches ranging from 1000 to 16 000 cores with linear scaling in terms of computing performance. Detailed chemistry and transport properties are derived using the software Cantera,⁶⁹ which implements the mixture-averaged transport model described by Kee *et al.*⁷⁰ The reaction rates of the multiple involved species were calculated with the finite rate method using a complex chemical mechanism. More specifically, the skeletal mechanism for methane combustion developed by Slavinskaya *et al.*,⁷¹ consisting of 21 species and 97 reactions, was used. This reaction mechanism was developed aiming for space propulsion applications with high combustion chamber pressures. This mechanism has been extensively used for the research of methane combustion in the frame of rocket engines.^{14,72} The relevant combustion parameters are summarized in Table II. The time step of the simulations is calculated in an adaptive way to ensure that the acoustic Courant–Friedrichs–Lewy (CFL) number remains below unity through all the domains. Since the maximum Mach number is on the order of $Ma \approx 0.3$, the maximum convective CFL number is roughly 0.3 as well. This low value coupled with a cubic discretization scheme has been proved to suppress most of the numerical dissipation.⁶⁸ With this configuration, the resulting time step ranges from 3.5 ns in the highest resolution simulation to 22.5 ns in the coarsest. These time steps deliver the maximum Fourier numbers on the order of $Fo \approx 0.3$ for the highest resolution simulation and $Fo \approx 0.05$ for the coarsest case. In both extremes, the time steps are substantially smaller than the chemical timescales, ensuring an adequate numerical integration of the species conservation equation.

Several simulations were conducted with varying resolution to study the sensitivity of the turbulent statistics to the grid size Δx . Details concerning each simulation are provided in Table III. The alphabetical order of the simulations is aligned with the resolution. Figure 2 was elaborated to illustrate the resolution level of each simulation. Here, the instantaneous mass fraction of carbon dioxide near the injection is displayed. The coarseness of simulations A and B is quite evident close to the inlet. For $z/\delta_{L0} \approx 70$, simulation SB appears to resolve the flame front as well as SC and SD. This is caused by the flame front thickening as the mixture moves far away from the injection. To a first approximation, simulations SC and SD seem

TABLE III. Summary of the performed simulations.

Simulation	Number of cells (x y z)	Saved time steps	Computational cost (MCPUh)
SA	48 × 32 × 480	700	0.01
SB	96 × 64 × 960	700	0.15
SC	216 × 144 × 2160	700	3.48
SD	288 × 192 × 2880	210	3.2

indistinguishable. This statement can be true for final species, such as carbon dioxide, which have gradients on the order of $1/\delta_{LO}$. Nevertheless, if intermediate species are considered, relevant differences between SC and SD near the injection may arise. The results were stored every $1 \mu s$, which roughly corresponds to eight times per eddy turnover time of the reactants. Every saved time step contains velocity, density, pressure, species concentration, and mass/thermal diffusivity for every cell in the main simulation domain. 700 time steps were recorded for the simulations SA, SB, and SC, which ensures an ergodic dataset. For simulation SD, only 200 time steps are available due to its high computational cost. Additional information concerning the statistical error and its spatial distribution is provided in Sec. V.

B. Post-processing strategy

The analysis of DNS databases consists of determining statistical parameters using a collection of instantaneous flow fields. The spatial distribution of every relevant physical parameter is available for every recorded time step. An example of such a result can be visualized in Fig. 3. The goal of post-processing is converting these individual

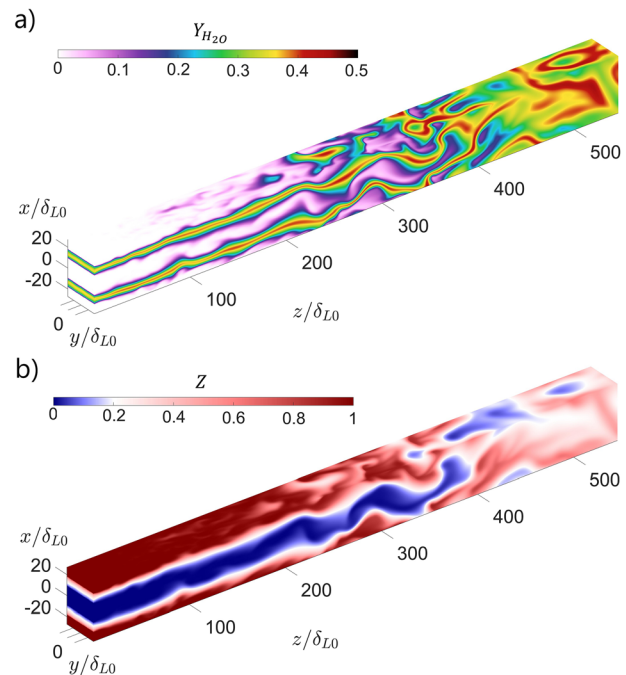


FIG. 3. Example of instantaneous field results: Water mass fraction (a) and mixture fraction (b).

results into meaningful statistical parameters. This section discusses this procedure and the resolution requirements.

1. Stationary turbulent flame simulation

The simulation of stationary flames involves transient processes that must be ruled out to ensure the quality of the statistics. The most important one is the ignition transient, in which the flow characteristics are not relevant to this study. Ignition is achieved by enforcing the adiabatic flame temperature in the injection post walls. This boundary condition only lasts for few microseconds, enough to achieve stable flame anchoring. Afterward, the boundary condition at the post-tip is set back to the original setup. The starting of combustion generates supersonic flow conditions, and high pressures take place. Only data significantly after this process should be used for averaging. A lapse of time equivalent to twice the reference residence time t_r is simulated after ignition before data are collected. This residence time is estimated as $t_r \approx L_Z/U_i = 120 \mu s$ with L_Z being the axial length of the domain (i.e., 3 mm). It is important to remark that this value overestimates the actual residence time since the average axial velocity is significantly larger due to the flow acceleration driven by thermal expansions. Since the ignition transient is computationally expensive, it is only performed in the lowest resolution simulation (i.e., SA). After this simulation reaches stationary conditions, the resulting physical fields are interpolated to generate starting conditions at a higher resolution. Since these interpolated fields are strongly tied to their low-resolution origin, it is necessary to allow for an additional transition into the higher-resolution flow characteristics. For this reason, an additional t_r is simulated at the increased resolution before the fields can be deemed

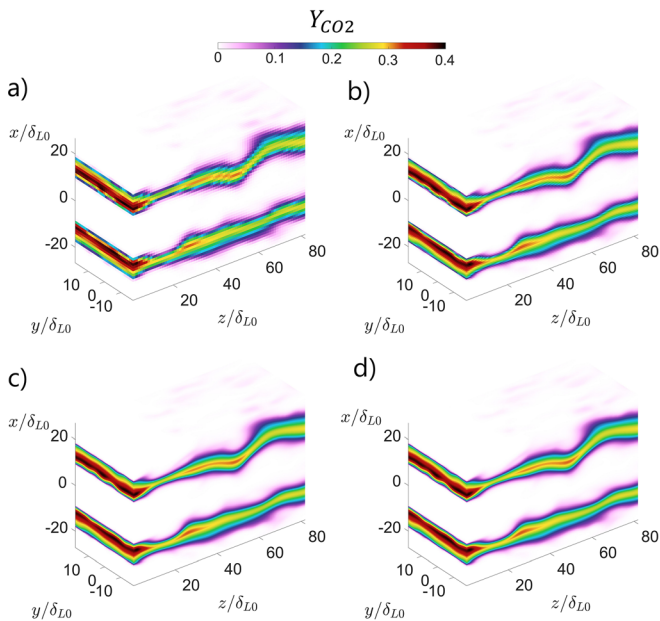


FIG. 2. Instantaneous carbon dioxide mass concentration with varying resolutions: Simulation SA (a), simulation SB (b), simulation SC (c), and simulation SD (d).

16 April 2024 11:36:10

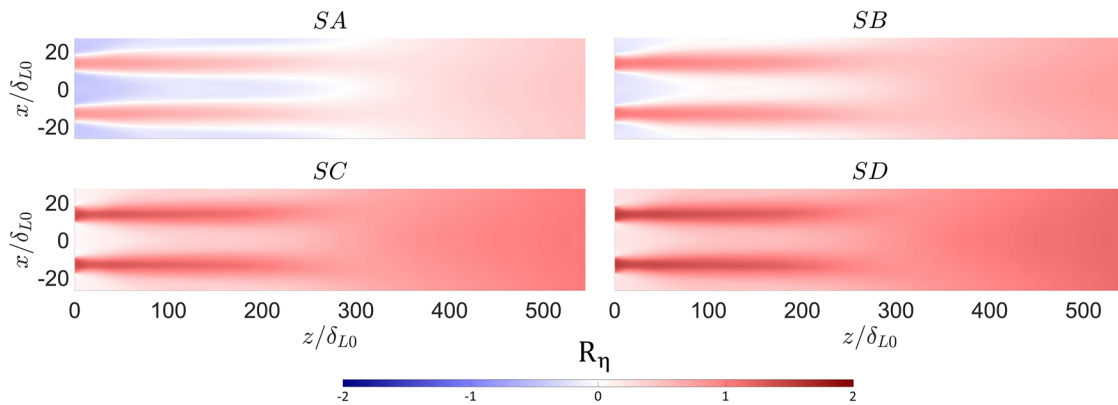


FIG. 4. Kolmogorov scale resolution quality for the performed simulations.

valid. Afterward, the data can be rendered as stationary, and it is used for calculating turbulent statistics.

2. Spatial transport of turbulent statistics

In the most general case, the turbulent flow statistics vary in each direction. However, within the performed simulations, the transport of turbulent properties is restricted in space. Since the statistics of the boundary conditions are constant across Y, invariant flow stochastics can be assumed therein. Symmetry is another relevant feature of the performed simulations. The flow statistics for the inlet and outlet boundary conditions are symmetric and periodic in X. Hence, it is possible to consider symmetry with respect to the center of oxygen or methane injection. The center of oxygen injection is chosen as the symmetry axis and is taken as the origin for the x coordinate to resemble the typical coaxial injection systems. Hence, the turbulent statistics in space are only a function of the distance to the injection center and the axial coordinate, i.e., $f(|x|, z)$. We can take the advantage of this condition to maximize the usage of the available data. For a mesh with $n_x \times n_y \times n_z$ cells in which n_t time steps are recorded at each position $\vec{s} = (\pm x, z)$, statistics are calculated using $2n_y n_t$ measurements.

3. Resolution requirements

The high computational cost of DNS arises from the need to resolve all relevant processes in space. In reacting flows, there are two critical phenomena requiring sufficient resolution. These are the flame front thickness and the smallest eddies, i.e., the Kolmogorov scale. Since these values largely vary, the assessment of the mesh quality must be done over space. The resolution of these processes is discussed in this subsection.

For simulation to be considered as DNS, a minimum resolution of the Kolmogorov eddies with $3/(2\pi)$ cells it is expected.^{40,41} To assess the degree of conformance with this requirement, the following performance parameter is defined:

$$R_\eta = \log_{10} \left(\frac{2\pi \cdot \eta}{3\Delta x} \right). \quad (20)$$

Therefore, $R_\eta \geq 0$ indicates compliance with the resolution of the smallest eddies and negative values otherwise. The resolution of the Kolmogorov scale was evaluated using this indicator throughout the domain. The results are displayed in Fig. 4. As can be seen, the mesh presents a sufficient resolution for simulations SC and SD. For the coarser resolution simulations, the flow is well resolved toward the products, but the grid size is not small enough near the injection. Overall, the resolution is enough for most of the domain. This is caused by the fact that the eddies grow as the combustion process progresses due to thermal expansions. Indeed, the Kolmogorov scale varies for over two orders of magnitude within the simulated domain.

From the standpoint of chemistry, it is required to resolve the flame front with enough cells to capture the dynamics of the local combustion process. In premixed turbulent combustion, it is recommended to use a grid size small enough to resolve the laminar flame front thickness with 10–20 cells.^{20,21} This criterion finds difficult application in turbulent diffusion flames since the flame front thickness greatly changes over space as mixing and combustions evolve in parallel. The instantaneous flame front thickness can be assessed using the gradient of the progress variable

$$\delta_c(x, y, z, t) = \frac{1}{|\nabla c(x, y, z, t)|}. \quad (21)$$

This value greatly changes over space and time, as can be observed in Fig. 5. In this graph, the instantaneous flame front thickness can be observed in a 2D cut of the main simulation. The values are normalized with the value at stoichiometric conditions since this scale can be taken as a reference for the thinnest achievable flame. The thinnest values are obtained near the injection, where $\delta_c \approx 3\delta_{L0}$. Further

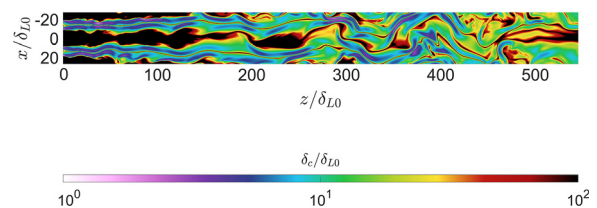


FIG. 5. Example of instantaneous reaction zone thickness.

downstream, the realized flame fronts are at least one order of magnitude greater than the flame thickness at stoichiometric conditions.

To characterize the flame front thickness at a given position in space, the instantaneous values are averaged over time and directions with no transport of statistics. In the scope of this work, this operation can be expressed as follows:

$$\bar{\delta}_c(x, z) = \frac{1}{\int_0^t \gamma(c) dy dt} \int_0^t \delta_c(x, y, z, t) \gamma(c) dy dt, \quad (22)$$

where $\gamma(c)$ is a top-hat filter used to restrict the analysis to mid-flame positions. This filter was defined in this work as follows:

$$\gamma(c) = \begin{cases} 1 & \text{if } 0.4 < c < 0.6, \\ 0, & \text{else.} \end{cases} \quad (23)$$

The usage of this sort of filtering prevents the consideration of data toward reactants or products. The progress variable presents significantly smaller gradients in these extremes, yielding artificially larger flame fronts. Hence, confining the analysis to medium progress variables ensures a realistic characterization of the flame length scale. The filtered average can be used to define an analog indicator for the flame front resolution

$$R_c = \log_{10} \left(\frac{0.1 \bar{\delta}_c}{\Delta x} \right). \quad (24)$$

This parameter was evaluated through all the domains for all simulations to assess the quality of the flame front resolution. The results are displayed in Fig. 6. For the sake of brevity, only SA and SB are displayed since $R_c > 0$ through all the domains for simulations SC and SD. As it can be seen, the worse resolution occurs near the injection since the flame front is thinner in this region. This is the consequence of the flow recirculation processes, which enable mixing conditions near stoichiometric. The resolution improves as one moves further downstream. This behavior follows the flame front thickening, and it is in good agreement with the trend observed in Fig. 5. It is important to remark that the value R_c was not calculated at certain positions close to the injection. This is due to the

fact that medium values of the progress variable were not observed. Hence, the filter $\gamma(c)$ presented only zero values disabling the possibility of averaging the data. This absence of recorded intermediate values for the progress variable indicates that the reacting features of the flow are of minor relevance. Hence, the flame front resolution bears little relevance in such places. Indeed, it can be seen that the regions lacking R_c measurements match quite well the positions where $\bar{\delta}_c \geq 100 \delta_{L0}$ in Fig. 5.

Although the flame front resolution requirements are fulfilled in average terms for the highest resolution simulations, certain flame instantiations are insufficiently resolved. A complete resolution in space and time of the flame front would imply prohibitive computational costs. The effect of these local inaccuracies is evaluated in integral terms with the mesh sensitivity analysis discussed in Sec. V.

IV. RESULTS

This section discusses the most relevant results of the simulated turbulent flame. The main goal is to illustrate the detailed insight that are accessible using DNS and the potential of these simulations for space propulsion applications.

The spatial development of the progress variable and the mixture fraction is presented in Fig. 7. From injection to $z/\delta_{L0} \approx 200$, the presence of reactive shear layers originating from the injection posts can be clearly observed. The diffusion flame structure is unstable from $z/\delta_{L0} \approx 200$ to $z/\delta_{L0} \approx 300$. Further downstream, both shear layers collapse into a single structure.

The burning dynamics are significantly different before and after the collapse of the shear layers. To illustrate this point, the heat release rate was averaged over time. The result is presented in Fig. 8. In this graph, the total averaged \bar{q} [Fig. 8(a)] can be observed along with the contribution of endothermic processes \bar{q}_{end} [Fig. 8(b)]. The endothermic contribution is calculated as the average conditional to $\dot{q} < 0$, and it is defined to be positive so that $\bar{q} = \bar{q}_{exo} - \bar{q}_{end}$. Near the injection, most heat release occurs at the reactive shear layer, with the highest average values recorded near the mean stoichiometric line. As the flame moves downstream, the region with a high heat release rate becomes thicker. This results from the combination of two simultaneous processes:

- (1) The flame structure becomes larger as mixing propagates in the lean and fuel-rich edges.

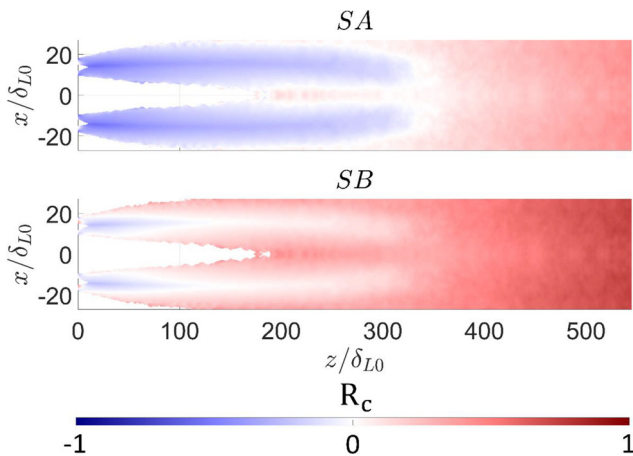


FIG. 6. Flame front resolution degree of completion R_c .

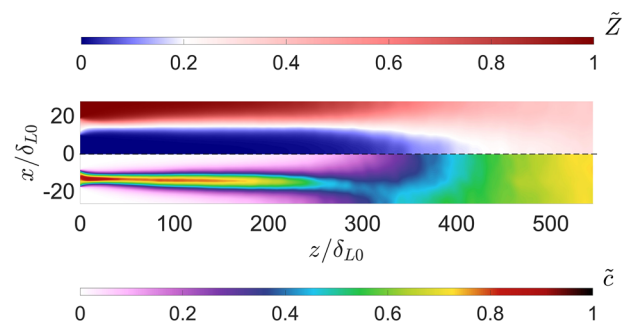


FIG. 7. Favre-averaged mixture fraction \tilde{Z} (top) and progress variable \tilde{c} (bottom).

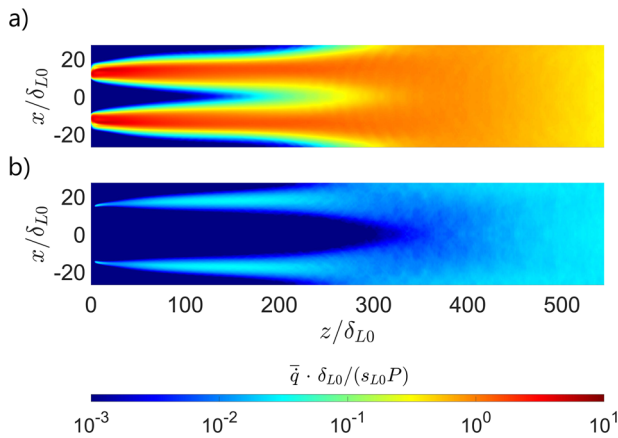


FIG. 8. Volumetric heat release rate: Mean value (a) and endothermic component (b).

(2) The shear layer oscillates around the mean stoichiometric line, expanding the regions where the burning processes become statistically relevant.

The first effect is typically well captured with standard combustion models. However, the second is more challenging as it involves somewhat counterintuitive processes, which are discussed as follows. By $z/\delta_{L0} \approx 70$, the oscillations of the flame structure become relevant enough to produce a decrease in the average variable \bar{c} at the stoichiometric line, as seen in Fig. 7. It is important to remark that this result does not imply an interruption or a reversal of the propellant's burning. Indeed, the radially averaged progress variable grows with a monotone tendency. The reason for the local progress variable drop is the increasing amplitude of the instantaneous stoichiometric line oscillations. This yields a smoothing of the average progress variable in the axial direction. Hence, the peak at the stoichiometric position decreases at the expenses of the nearby fuel-rich and lean regions. Figure 9 was elaborated to further illustrate the growth of the fluctuations with respect to the average stoichiometric line as the flame moves axially. As can be seen, close to the injection, the maximum stoichiometric composition and the maximum progress variable are very close to the average isoline of $Z = Z_{st}$. Separation between instantaneous and

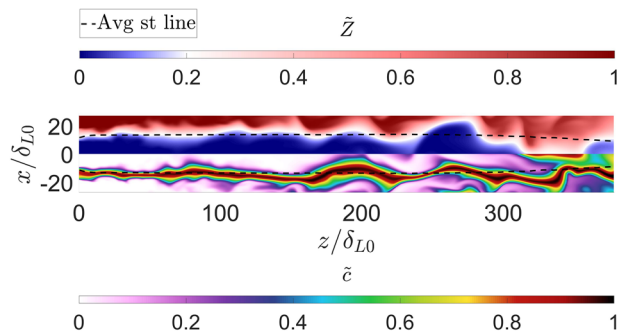


FIG. 9. Cross sectional cut of the instantaneous mixture fraction and the progress variable. The average stoichiometric isoline is displayed to illustrate the magnitude of the instantaneous oscillations.

averaged values become stronger as the flow displaces to the downstream positions. In the particular example displayed in Fig. 9, the merging of both shear layers can be observed by $Z \approx 350 \delta_{L0}$.

In average terms, flame oscillations reach the order of magnitude of the distance between the injection posts by $z/\delta_{L0} \approx 300$. This precipitates the collapse of the shear layers, which merge into a single structure. The described process can be observed in the instantaneous fields represented in Figs. 1(b) and 3(a). The turbulent combustion dynamics in this zone are quite challenging to capture. As the shear layer becomes unstable with significant flame-generated turbulence, chemistry cannot adapt instantaneously to the fluctuations in the flame structure. This violation of core flamelet assumptions leads to sporadic quenching,^{43,73,74} which can be observed through the relative growth of \bar{q}_{end} with respect to the overall heat release rate. The merging of the twin shear layers marks the beginning of a region in which combustion primarily occurs in the fuel-rich premixed conditions, with significantly slower combustion progress. These larger chemical timescales are motivated by the fact that a large fraction of the reactants has already been consumed by this point. In addition, the mean flow velocity is significantly higher compared to near the injection, reducing the residence time of the molecules for the same unit of length. The contribution of endothermic reactions near the domain's outlet is also motivated by molecular recombinations. Due to the initial combustion in the lean and stoichiometric conditions, products present a mixture fraction below the global value, with an excessive presence of carbon dioxide. This product is partially converted into carbon monoxide and oxygen to shift the composition to a fuel-rich chemical equilibrium. Hence, the burning of the remaining reactants is complemented by the recombination of the existing products. Several of the involved chemical reactions are endothermic, enabling the observed trend.

The performed simulations allow for detailed analyses of the interactions between the turbulent flow dynamics and combustion as well. To illustrate this possibility, the spatial evolution of the turbulent kinetic energy and its dissipation rate are displayed in Fig. 10.

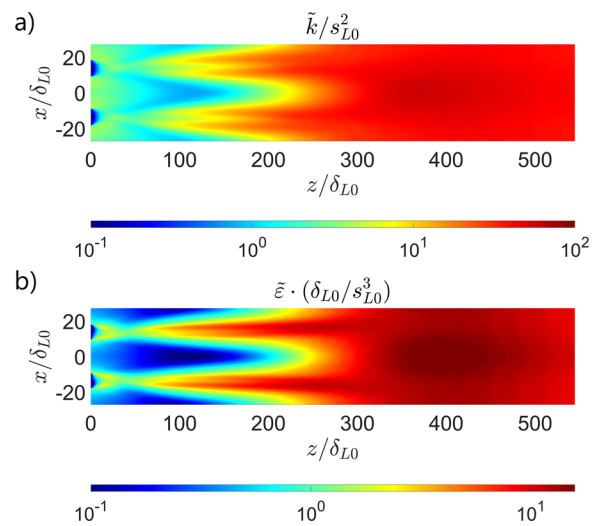


FIG. 10. Relevant turbulent parameters in the simulated diffusion flame: Turbulent kinetic energy (a) and dissipation rate of the turbulent kinetic energy (b).

In addition, the radially averaged turbulent kinetic energy transport budget is presented in Fig. 11. As it can be seen, the turbulent kinetic energy grows steadily in the region where the shear layers are present, reaching a local maximum following their collapse.

The initial TKE growth is mainly driven by the turbulent production through mean pressure gradients and the covariance between the fluctuating pressure gradients and velocity, i.e., T_2 and $T_3 + T_5$. These processes present similarities with what has been observed in the premixed flames with high Damköhler numbers.^{32,75} When chemical processes become very fast compared to turbulence, fluctuations in density are coupled with the flow's acceleration, enabling non-zero values for $\overline{u'v'}$. This condition enables the conversion of the mean pressure gradients into the turbulent kinetic energy through T_2 . In addition, the fast chemistry in the shear layer enables the generation of flame front wrinkling, driving the negative coupling between the pressure gradient fluctuations and the velocity fluctuations.⁷⁶ This phenomenon produces turbulence as $T_3 + T_5 > 0$. This growth in turbulence is crucial to ensure the validity of the typical flamelet models. If the fluctuations in the shear layer become significantly faster than chemistry, the standard flamelet models are not able to predict the combustion statistics since they are coupled with turbulence. Identifying these situations is crucial to enable convenient corrections to the flamelet combustion models. The growing trend of TKE is interrupted by the collapse of the shear layers. At this position, the dissipation rate experiences a significant increase due to the merging of clusters with very different physical properties. Turbulence-generation terms cannot keep up with the dissipation rate after this point. The main reason is the limitation of the incoming burnable flow, since the edges of the shear layers are no longer surrounded by the fresh reactants but by the complementary shear layer. Consequently, the combustion progress is significantly slowed down in this region. This impairment increases the chemical time-scales, enabling the interference of vortical structures in the processes that facilitated turbulence generation near the injection. Consequently, the contributions of T_2 and $T_3 + T_5$ decrease, and turbulence annihilation due to viscosity becomes dominant. The simulation domain is not large enough to reach the flow state in which $|T_4| \approx |T_2 + T_3 + T_5|$. Nonetheless, this scenario is expected when $\tilde{c} \approx 1$ as chemical reactions become residual.

Conventional RANS solvers can hardly capture the complex interactions reported in this work. The generation of turbulence due to coupled pressure gradients and velocity fluctuations is neglected in

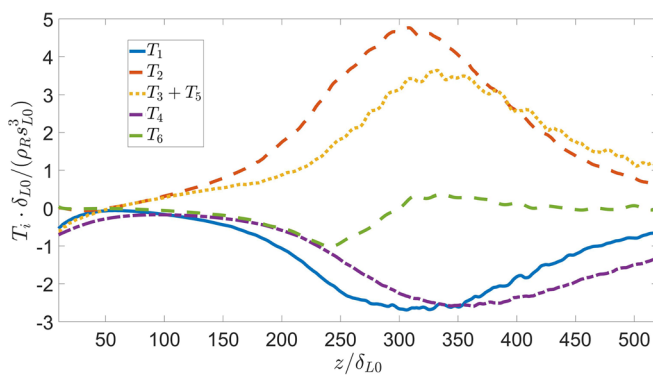


FIG. 11. Radially averaged turbulent kinetic energy transport budget.

most commercial solvers and models.^{20,36,77,78} Furthermore, the decrease in the mean progress variable due to oscillations in the flame structure cannot be observed in most combustion models, which rely on the simple first- or second-order turbulent statistics. These phenomena play an important role in the development of the reacting flow and are crucial for engine performance predictability.

V. UNCERTAINTY ANALYSIS

As mentioned in the introduction, one of the challenges involving the usage scale-resolving simulations is their error assessment. This section addresses this issue through the evaluation of the uncertainties surrounding the performed numerical simulations. In turbulent flow, the physical variables continuously fluctuate. Therefore, the expected outcome from a numerical simulation is not a fixed value, but a probability distribution function for the variables. From a strict point of view, the assessment of the error should be done in terms of deviations between the measured and real probability distributions. However, this approach would be impractical for most variables. For this reason, the statistical behavior of the turbulent quantities is summarized with their average value, which is the most relevant result in most engineering applications. Another important assumption done in this work is that statistics do not vary at a sub-grid level. In high-resolution simulations, this premise is correct since the grid size is small enough to capture the smallest turbulent structures, and the gradients of average values are always very small compared to those of instantaneous ones. This is the case for the simulations performed within this work. However, in certain coarse LES, it could be claimed that the statistics vary within a given cell. A more general approach would be required in such a case.

Two different analyses are presented in this section. First, a novel method for the estimation of the error scale based on the simulated time is introduced and validated. Second, a mesh sensitivity analysis is performed to evaluate the influence of resolution on the quality of the measured turbulent statistics.

A. Error estimation method

Estimating the error due to insufficient data is an inherent challenge in scale-resolving simulations. High accuracy in the measured statistics requires long simulation timespans, with subsequently high computational cost. Therefore, professionals aim to find a compromise that enables statistical convergence with minimum simulation time. In DNS for turbulent combustion, it is often considered that averaging several eddy turnover times guarantees an ergodic database. However, this criterion is rather arbitrary, and the number of simulated turnover times greatly varies in the scientific literature. In addition, the reference turnover time usually corresponds to that of the reactants. If combustion slows down turbulence, this becomes a spurious indicator since the limiting process would correspond to the products. This section introduces a method analog to the classical statistical inference to enable an objective quantification of the error due to insufficient recorded data. The main idea is to derive a suitable normalization of the averaging error and study its probability distribution. If the defined error expression is correct, the distribution shall be universal. This will enable an accurate estimation of the error margins with specific confidence intervals.

In the inference theory, the normalized error is denoted as the t -value, and it is defined as follows:²⁵

$$t = \frac{q^\epsilon}{\sigma_q} \sqrt{n}, \tag{25}$$

where q^ϵ is the offset between the actual average and the measured one, σ_q is the measured standard deviation, and n is the number of individual measurements. We shall derive a similar expression for Favre-averaged variables in a turbulent flow, which we will be referred to as the pseudo t function t_{ps} . The first step requires the definition of the statistical error. For a given number of measurements n , the error is evaluated as follows:

$$\tilde{q}^\epsilon = |\tilde{q}^*(n) - \tilde{q}|, \tag{26}$$

where $\tilde{q}^*(n)$ denotes the estimated Favre-average using n consecutive measurements. The standard formulation of the t function assumes that all measurements are independent. This is not necessary the case in recorded data of a direct numerical simulation. If turbulent structures present a lifetime greater than the time between two measurements, independence cannot be assumed. Furthermore, averaging over space is often done in the directions with no transport of statistics. Although this strategy allows using a larger amount of data, the proximity of the measurements limits their independency. These effects require the application of appropriate corrections that account for them. For a simulation with n recorded time steps, a sampling frequency f_s in which the data are averaged in a direction with length l_p , it is possible to estimate the pseudo degrees of freedom as follows:

$$n_{ps} = \frac{n}{f_s t_{DC}} \left(\frac{l_p}{l_{DC}} \right)^s, \tag{27}$$

where t_{DC} and l_{DC} are the necessary time and length for the measurements to be considered independent. The exponent s accounts for the number of directions used for spatial averaging. Within this work, $s = 1$ is taken since the spatial average is performed over a single direction (Y). For simulations of turbulent premixed turbulent flames in the absence of walls, the flow is usually statistically planar,⁷⁹ yielding $s = 2$. One evident conclusion from this expression is that an excessively high sampling frequency alone does not guarantee sufficient recorded data. If $t_{DC} f_s \gg 1$, the observations are too close, and no new information is obtained with consecutive measurements. Similarly, if l_p and l_{DC} are in the same order of magnitude, the statistics hardly improve, thanks to spatial averaging. However, unlike in time average $l_p/l_{DC} > 1$, so there is always at least a small benefit in using space averaging. At this point, it is necessary to obtain realistic values for the independent time and length scales. In a turbulent flow, these scales can be taken as one of the largest eddies. Hence, $t_{DC} \approx t_T$ and $l_{DC} \approx \bar{L}$ are assumed. This consideration yields the following expression for the pseudo degrees of freedom:

$$n_{ps} = \min \left(n \frac{l_p^s \bar{L}^{1+s}}{f_s k^{1+(3/2)s}}, n \frac{l_p^s \bar{L}^s}{k^{(3/2)s}} \right). \tag{28}$$

The minimum condition is stated to account for the scenario in which the sampling frequency is smaller than the vortical frequency, thereby securing independency between the consecutive measurements. An analogue condition is not realistic for the space correction, since the largest eddies are smaller than the domain size. The choice of the sampling frequency is an interesting design problem that requires commenting. Low simulation frequencies maximize the usability of the

recorded data since independence between the measurements is ensured. This is optimal from the standpoint of data storage since a minimal amount of results must be saved. However, a longer simulation time is required, increasing the computational cost. For this reason, high sampling frequencies are usually preferred due to their affordability in computational terms. Nevertheless, an upper limit for f_s exists as well. The storage requirements grow with the sampling frequency, hindering data management. Moreover, the reconstruction of parallelized meshes demands additional computational costs, which can mask the gains of a lower simulation time. In the experience of the authors, the optimal sampling frequency is on the order of twice that of the large eddies with the smallest timescale, i.e., $f_{s,opt} \approx 2 \min \left(\frac{k}{\bar{L}} \right)$.

Under all the previously stated considerations, it is now possible to state the following expression for the pseudo t function:

$$t_{ps} = \frac{\tilde{q}^\epsilon}{\tilde{\sigma}_q} \sqrt{n_{ps}}. \tag{29}$$

In the classical inference theory, the PDF of t follows the so-called student-distribution, and it is only a function of the degrees of freedom n . In practice, the t distribution has little sensitivity on the degrees of freedom for $n > 30$. For this reason, this dependency will be neglected in the current analysis. The probability distribution of the pseudo t function was obtained numerically for several relevant parameters. Only data with large enough degrees of freedom ($n_{ps} \geq 30$) were considered to ensure independency on the degrees of freedom. The result is presented in Fig. 12. As it can be seen, the distribution appears to be universal, with minor discrepancies between the various considered variables.

The only variable exhibiting a noticeable deviation is the Favre-averaged mass fraction of carbon monoxide \tilde{Y}_{CO} . The reason for this mismatch is the high skewness of this variable's pdf. Since the mean value is close to zero and negative values are not possible, the pdf of ρY_{CO} is strongly skewed toward the right. In such a case, the deviations from the classical theory are further accentuated. The main practical effect is that the standard deviation overestimates the fluctuations of this variable around the mean. This results in smaller pseudo t -values, increasing the concentration of data toward $t = 0$. The commonly used t -values are presented in Table IV. As it can be seen, the values are very similar for each variable with the exception of carbon

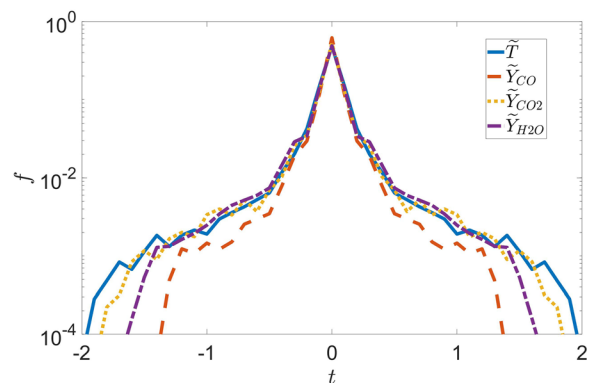


FIG. 12. Numerically obtained probability density function of the t -value for relevant variables in turbulent combustion.

TABLE IV. Pseudo t-values for different confidence intervals of the most relevant combustion statistics ($n_{ps} \geq 30$).

	80%	90%	95%	99%
\tilde{T}	0.0753	0.176	0.347	1.12
\tilde{Y}_{CO_2}	0.0639	0.175	0.345	1.05
\tilde{Y}_{H_2O}	0.071	0.187	0.371	0.971
\tilde{Y}_{CO}	0.0475	0.099	0.236	0.663

monoxide, which presents substantially smaller results due to the mentioned high skewness.

The obtained t-values are smaller than those used in the classical inference tables. This is probably caused by the fact that taking the large eddies timescale is a worst-case assumption. It would be more accurate to consider the integral length scale $\tilde{\Lambda}$ and the integral timescale $\tilde{\Lambda}/u_{rms}$. These scales are smaller than their counterparts for large eddies, i.e., \tilde{L} and t_T . Consequently, the method described here underpredicts the pseudo degrees of freedom, yielding smaller t-values. Although integral scales are more precise, their calculation is substantially more complex, especially in the variable-density flows. For this reason, the usage of large eddy scales is advised for turbulent combustion applications. The obtained pseudo t-values for the variables that adhere to the main trend can be taken as a reference and be used generally. Some variables, such as \tilde{Y}_{CO} , may deviate due their highly skewed distributions. Nevertheless, in such cases, using the reference values will overestimate the error, effectively increasing the confidence interval. In other words, using the reference values will provide accurate error boundaries in the best case and will overestimate the error in the worst scenario.

As displayed in Table IV, the value $t_{ps} \approx 0.354$ guarantees a confidence interval greater than 95% for most variables. Therefore, it is possible to derive the following expression for the statistical error if the sampling frequency is larger than the turbulence timescale:

$$\tilde{q}_{95\%}^e \approx 0.354 \frac{\tilde{\sigma}_q}{\sqrt{t_s} I_p} \frac{\tilde{k}^{\frac{2+3s}{4}}}{\tilde{c}^{\frac{1+s}{2}}}. \quad (30)$$

This expression is extremely useful in the planning of numerical simulations. Using known RANS results, it is possible to estimate the needed simulation time t_s , and, thus, obtain a rough assessment of the computational costs. For on-going simulations, Eq. (30) can be used to determine the additionally required simulation time to obtain an error below the target one. To illustrate this point, an example of the actual and estimated error is provided in Fig. 13. The top of this graph shows the actual error in averaging the flow temperature, whereas the bottom represents the estimated error with a confidence interval of 95%. As can be seen, the error scale provides a consistent estimation of the ceiling of the actual one. Furthermore, the problematic regions are accurately identified, which is valuable information for evaluating the results.

B. Mesh sensitivity analysis

A mesh sensitivity analysis was performed comparing the obtained statistics with varying resolutions in the numerical

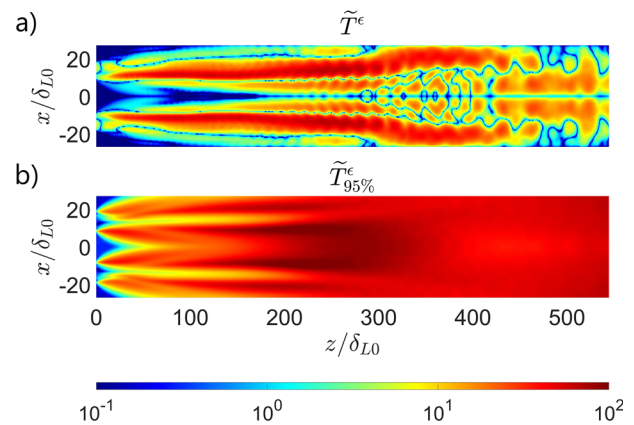


FIG. 13. Example of error with confidence intervals: Actual error in average temperature (a) and estimated temperature error with a confidence interval of 95% (b).

simulations. The main goal of this study is to assess the validity of the standardized requirements for the grid size and the overall influence in the simulation accuracy. Figure 14 illustrates the obtained radially averaged mean values for several physical variables. Despite the lower amount of data, the results of simulation SD are suitable to be used in this sort of analysis since the radial averaging compensates the insufficient amount of data for accurate spatial statistics. As it can be seen, the differences are marginal toward through most of the flame, and they are likely to be driven by averaging error rather than differences in resolution.

The most substantial differences can be appreciated toward injection in simulation SA. To further investigate the reasons for these discrepancies, the error is studied spatially. Figure 15 was elaborated for this goal. This graph displays the offset between the statistic in the coarse resolution simulations and the high-resolution case. Here, the results in coarse resolution are compared with the statistics in a high-resolution simulation. The reference (i.e., high-resolution) simulation is SC instead of SD, although it is coarser. The reason for this is that the obtained spatial statistics in simulation SD are not suited for this sort of analysis since not enough time steps were recorded due to the high computational cost. As it can be seen, most of the discrepancies take place in the recirculation zone. The coarse simulations underpredict the presence of products in this region, although a higher prevalence is predicted shortly downstream. The insufficient flame front resolution discussed in Sec. III is the most probable cause for these discrepancies. Since chemical changes are enforced within a small number of cells, the mass fraction gradients are smoothed. As a consequence, a smaller concentration of products is obtained toward the beginning of combustion and larger progress variable afterward. In any case, it is important to keep in mind that the differences are overall small after the injection post. In addition, the regions with higher discrepancies present a density one order of magnitude below that of reactants. This limits the propagation of these errors into the overall flow dynamics.

Based on the observed results, a grid size small enough to resolve the laminar flame front at stoichiometric conditions δ_{L0} with 3–4 cells appears to ensure sufficient accuracy in the results. This is mainly caused by the fact that the actually realized flame thickness is at least

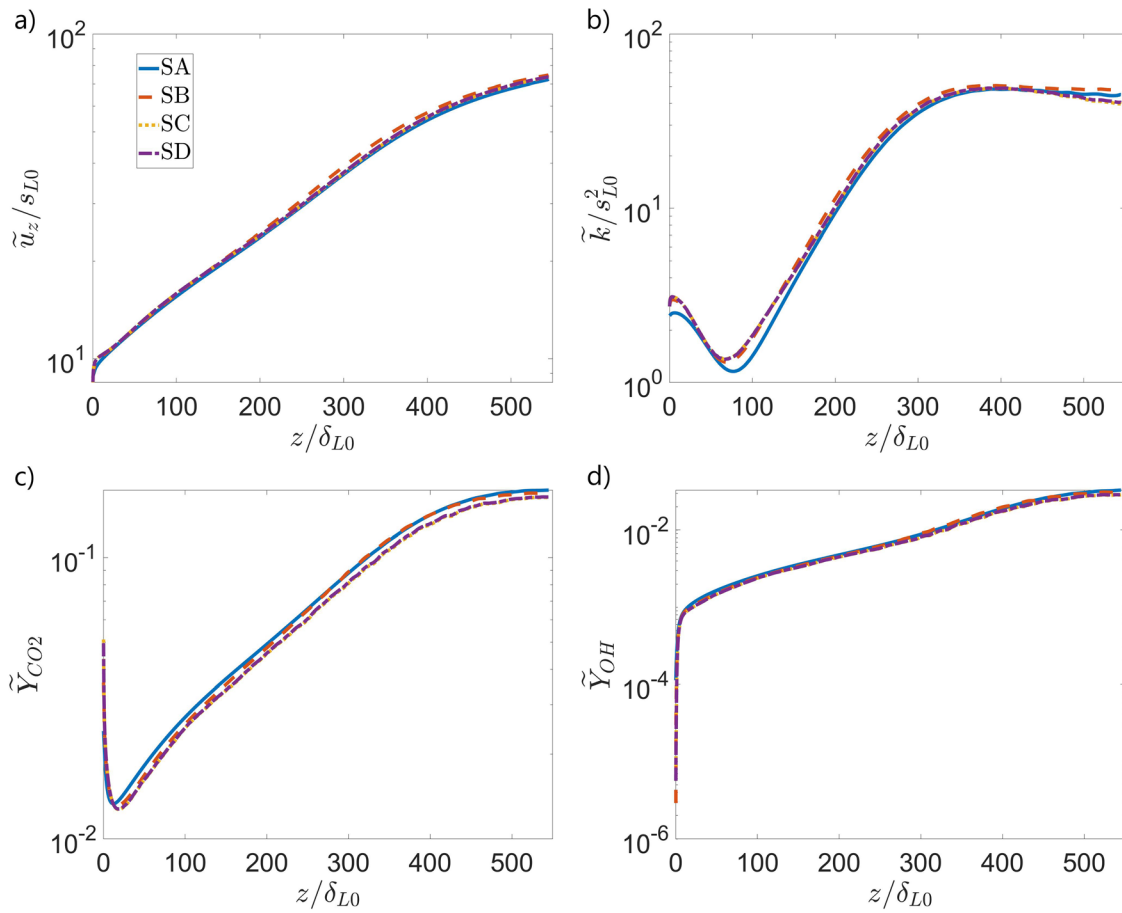


FIG. 14. Radially averaged values of relevant turbulent variables for the performed simulations: Favre-averaged axial velocity \tilde{u}_z (a), Favre-averaged turbulent kinetic energy \tilde{k} (b), Favre-averaged mass fraction of carbon dioxide \tilde{Y}_{CO_2} (c), and Favre-averaged mass fraction of hydroxyl \tilde{Y}_{OH} (d).

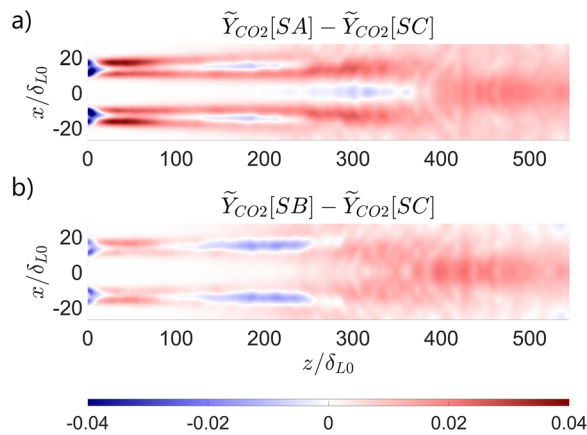


FIG. 15. Spatial distribution of the carbon dioxide concentration error: Comparison between SA and SC (a) and comparison between SB and SC (b).

three times larger than δ_{L0} . This condition ensures that most of the relevant dynamic chemical processes can be accurately resolved with a grid size in the order $\Delta x \approx \delta_{L0}/4$.

VI. CONCLUSIONS

A turbulent methane–oxygen diffusion flame at high pressure was simulated and post-processed using DNS. The simulation setup aimed to represent the mixing and combustion in the injection region of a modern rocket combustor. The domain length does not allow to simulate the entire combustion chamber. Nevertheless, it suffices to observe phenomena that are not accessible with the conventional methods but play a major role in the development of the turbulent reacting flow. One of these processes is turbulent generation through the correlation between the pressure gradients and the velocity fluctuations. Exotic effects in the transport of species were reported as well. For example, negative transport of the progress variable due to the fluctuations in the flame structure was observed.

The convergence of turbulent statistics was studied using the available data. A method to estimate the averaged error is proposed, based on the classical statistical inference theory. It is found that the error in the measured average values asymptotically tends to zero as it is inversely proportional to the square root of the number of samples. An expression dependent on the local turbulence characteristics is derived to estimate the local error. The resolution requirements were investigated as well. With the available results, it is estimated that a grid size able to resolve the laminar flame front at stoichiometric conditions with three to four cells ensures convergence as further mesh refinements yield variations in the results below 1%. This result is primarily motivated by the larger size of chemical scales. In a turbulent diffusion flame, the reaction zone is significantly thickened compared to the laminar premixed case, presenting gradients of properties 3–10 times smaller. In addition, the thinnest flamelets play a minor contribution due to their lower density, limiting their influence in the overall turbulent flow dynamics. However, it is important to keep in mind that the local errors can rise up to one order of magnitude greater than the averaged ones.

The findings within the present research demonstrate the advantages of using DNS to investigate the turbulent flow dynamics for space propulsion applications. The performed uncertainty analysis will support future direct numerical simulations of turbulent diffusion flames, optimizing the computational resources and evaluating the error margin.

ACKNOWLEDGMENTS

The authors thank Super-MUC NGen for providing the computational resources for performing the numerical simulations and its post-processing. The authors are extremely grateful toward Martin Ohlerich for his support in optimizing the parallel calculations. The authors are also grateful for the funding by the project “H₂-O₂-Brennkammer im Kraftwerk” of “Bayerische Forschungsstiftung” with reference Grant No. AZ-1517–21.

AUTHOR DECLARATIONS

Conflict of Interest

The authors have no conflicts to disclose.

Author Contributions

Daniel Martinez-Sanchis: Conceptualization (lead); Data curation (lead); Formal analysis (equal); Investigation (equal); Methodology (equal); Project administration (equal); Resources (equal); Software (equal); Validation (equal); Visualization (equal); Writing – original draft (equal); Writing – review & editing (equal). **Andrej Sternin:** Conceptualization (equal); Funding acquisition (equal); Writing – original draft (equal); Writing – review & editing (equal). **Oskar Haidn:** Conceptualization (equal); Investigation (equal); Methodology (equal); Supervision (lead); Writing – original draft (equal); Writing – review & editing (equal). **Martin Tajmar:** Conceptualization (equal); Supervision (equal).

DATA AVAILABILITY

The data that support the findings of this study are available from the corresponding author upon reasonable request.

REFERENCES

- D. Haeseler, V. Bombelli, P. Vuillemoz, R. Lo, T. Marée, and F. Caramelli, “Green propellant propulsion concepts for space transportation and technology development needs,” in 2nd International Conference on Green Propellants for Space Propulsion, Chia Laguna (Cagliari), 2004.
- R. L. Sackheim and R. K. Masse, “Green propulsion advancement: Challenging the maturity of monopropellant hydrazine,” in 49th AIAA Joint Propulsion Conference, 2013.
- H. N. M. Ciezki and L. Werling, “Trends in research and development on green chemical propulsion for orbital systems,” in 7th International Conference on Recent Advances in Space Technologies, RAST 2015, Istanbul, Turkey, 2015.
- C. Scharlemann, “GRASP: Status and future of green propellants,” in Space Propulsion Conference, Bordeaux, France, 2012.
- T. Brown, M. Klem, and P. McRight, “Foundational methane propulsion related,” in Space Propulsion, Rome, Italy, 2016.
- O. Haidn, G. Ordonneau, S. Soller, and M. Onofri, “Oxygen–methane combustion studies in the in space propulsion programme,” in 4th European Conference for Aerospace Sciences, Saint Petesbourg, Russia, 2011.
- D. Kajon, D. Liuzzi, C. Boffa, M. Rudnykh, D. Drigo, L. Arione, N. Ierardo, and A. Sirbi, “Development of the liquid oxygen and methane M10 rocket engine for the Vega-E upper stage,” (published online 2019).
- B. Karlovitz, D. W. Denniston, and F. E. Wells, “Investigation of turbulent flames,” *J. Chem. Phys.* **19**(5), 541–547 (1951).
- K. N. C. Bray, P. A. Libby, G. Masuya, and J. B. Moss, “Turbulence production in premixed turbulent flames,” *Combust. Sci. Technol.* **25**(3–4), 127–140 (1981).
- D. R. Ballal, “Combustion-generated turbulence in practical combustors,” in *23rd Joint Propulsion Conference* (AIAA, 1987).
- A. Gulati and J. F. Driscoll, “Flame-generated turbulence and mass fluxes: Effect of varying heat release,” in *Symposium (International) on Combustion* (Elsevier, 1986).
- O. J. Haidn, M. P. Celano, M. Luo, C. Roth, S. Silvestri, and N. A. Slavinskaya, “On methane/oxygen combustion for rocket applications,” in *International Symposium on Innovation and Prospects of Liquid Propulsion*, Xi’an, 2016.
- D. Maestro, B. Cuenot, A. Chemnitz, T. Sattelmayer, C. Roth, O. J. Haidn, Y. Daimon, G. Frank, H. Müller, J. Zips, M. Pfitzner, R. Keller, G. Frank, M. Pfitzner, and L. Selle, “Numerical investigation of flow and combustion in a single-element GCH₄/GO_x rocket combustor: Chemistry modeling and turbulence-combustion interaction,” AIAA Paper No. 2016-4996, 2016.
- N. Perakis, D. Rahn, O. J. Haidn, and D. Eiringhaus, “Heat transfer and combustion simulation of seven-element O₂/CH₄ rocket combustor,” *J. Propul. Power* **35**(1), 1080–1018 (2019).
- L. Vervisch and T. Poinso, “Direct numerical simulation of non-premixed turbulent flames,” *Annu. Rev. Fluid Mech.* **30**, 655–691 (1998).
- L. Vervisch, P. Domingo, J. Reveillon, S. Payet, C. Pera, and R. Hauguel, “DNS and LES of turbulent combustion,” in *Computational Fluid Dynamics in Chemical Reaction Engineering IV*, Barga, Italy, 2005.
- I. Celik, M. Klein, and J. Janicka, “Assessment measures for LES applications,” in 14th International Conference on Nuclear Engineering, Miami, Florida, 2006.
- W. Rodi, “DNS and LES of some engineering flows,” *Fluid Dyn. Res.* **38**(2), 145–173 (2006).
- G. Pont, P. Brenner, P. Cinnella, and J.-C. Robinet, “High-order hybrid RANS/LES strategy for industrial applications,” in *Direct and Large-Eddy Simulation X* (Springer, Cham, 2018), pp. 313–319.
- T. Poinso and D. Veynante, “Introduction to turbulent combustion,” in *Theoretical and Numerical Combustion* (R. T. Edwards, 2005), pp. 125–181.
- A. Y. Poludnenko and E. S. Oran, “The interaction of high-speed turbulence with flames: Global properties and internal flame structure,” *Combust. Flame* **157**(5), 995–1011 (2010).
- S. B. Pope, “The statistical description of turbulent flows,” in *Turbulent Flows* (Cambridge University Press, 2000), pp. 34–82.
- M. Eckert, “Chaos and turbulence,” in *The Turbulence Problem* (Springer, 2019), pp. 75–85.

- ²⁴A. Favre, *Problems of Hydrodynamics and Continuum Mechanics* (SIAM, Philadelphia, 1969).
- ²⁵C. Heumann and M. S. Shalabh, "Inference," in *Introduction to Statistics and Data Analysis* (Springer Cham, 2016), pp. 181–205.
- ²⁶D. Bradley, "How fast can we burn?," *24th Symposium (International) Combustion* (Elsevier, 1992), Vol. 24, pp. 247–262.
- ²⁷N. Chakraborty, A. Herbert, U. Ahmed, H. G. Im, and M. Klein, "Assessment of extrapolation relations of displacement speed for detailed chemistry direct numerical simulation database of statistically planar turbulent premixed flames," *Flow, Turbul. Combust.* **108**, 489–507 (2022).
- ²⁸J. Furukawa, Y. Noguchi, T. Hirano, and F. A. Williams, "Anisotropic enhancement of turbulence in large scale, low intensity turbulent premixed propane-air flames," *J. Fluid Mech.* **462**, 209–243 (2002).
- ²⁹J. R. MacDonald and C. M. Fajardo, "Turbulence anisotropy investigations in an internal combustion engine," *J. Eng. Gas Turbines Power* **143**(9), 091011 (2021).
- ³⁰S. Zhang and C. J. Rutland, "Premixed flame effects on turbulence and pressure-related terms," *Combust. Flame* **102**(4), 447–461 (1995).
- ³¹S. Nishiki, T. Hasegawa, R. Borghi, and R. Himeno, "Modelling of flame-generated turbulence based on direct numerical simulations databases," *Proc. Combust. Inst.* **29**, 2017 (2002).
- ³²N. Chakraborty, M. Katragadda, and R. S. Cant, "Statistics and modelling of turbulent kinetic energy transport in different regimes of premixed combustion," *Flow, Turbul. Combust.* **87**, 205–235 (2011).
- ³³Z. Wang and J. Abraham, "Effects of Karlovitz number on turbulent kinetic energy transport in turbulent lean premixed methane/air flames," *Phys. Fluids* **29**, 085102 (2017).
- ³⁴B. L. Launder, G. J. Reece, and W. J. Rodi, "Progress in the development of a Reynolds stress turbulence closure," *J. Fluid Mech.* **68**, 537–566 (1975).
- ³⁵P. Domingo and K. N. C. Bray, "Laminar flamelet expressions for pressure fluctuation terms in second moment models of premixed turbulent combustion," *Combust. Flame* **121**, 555–574 (2000).
- ³⁶ANSYS, Inc., *ANSYS Fluent Theory Guide* (ANSYS, Inc., 2013), p. 15317.
- ³⁷D. Martínez-Sanchis, S. Banik, A. Sternin, D. Sternin, O. Haidn, and M. Tajmar, "Analysis of turbulence generation and dissipation in shear layers of methane-oxygen diffusion flames using direct numerical simulations," *Phys. Fluids* **34**, 045121 (2022).
- ³⁸K. N. C. Bray, "The challenge of turbulent combustion," in *Symposium (International) on Combustion* (Elsevier, 1996).
- ³⁹S. B. Pope, "The scales of turbulent motion," in *Turbulent Flows* (Cambridge University Press, Cambridge, 2000), pp. 182–263.
- ⁴⁰P. K. Yeung and S. B. Pope, "Lagrangian statistics from direct numerical simulations of isotropic turbulence," *J. Fluid Mech.* **207**, 531–586 (1989).
- ⁴¹S. B. Pope, "Direct numerical simulation," in *Turbulent Flows* (Cambridge University Press, 2000), pp. 344–357.
- ⁴²C. K. Law, "Conservation equations," in *Combustion Physics* (Cambridge University Press, 2006), pp. 157–193.
- ⁴³B. Cuenot, "The flamelet model for non-premixed combustion," in *Turbulent Combustion Modelling: Advances, New Trends and Perspectives* (Springer, 2011), pp. 43–61.
- ⁴⁴A. Najafi-Yazdi, B. Cuenot, and L. Mongeau, "Systematic definition of progress variables and intrinsically low-dimensional, flamelet generated manifolds for chemistry tabulation," *Combust. Flame* **159**, 1197–1204 (2012).
- ⁴⁵K. Bray, P. Domingo, and L. Vervisch, "Role of the progress variable in models for partially premixed turbulent combustion," *Combust. Flame* **141**(4), 431–437 (2005).
- ⁴⁶N. Peters, *Turbulent Combustion* (Cambridge University Press, Cambridge, 2001).
- ⁴⁷R. W. Bilger, "Turbulent jet diffusion flames," *Prog. Energy Combust. Sci.* **1**(2–3), 87–109 (1976).
- ⁴⁸C. D. Pierce and P. Moin, "Progress-variable approach for large-eddy simulation of non-premixed turbulent combustion," *J. Fluid Mech.* **504**, 73–97 (2004).
- ⁴⁹T. Zirwes, F. Zhang, P. Habisreuther, M. Hansinger, H. Bockhorn, M. Pfitzner, and D. Trimis, "Identification of flame regimes in partially premixed combustion from a quasi-DNS dataset," *Flow, Turbul. Combust.* **1006**, 373–404 (2001).
- ⁵⁰T. Seitz, A. Lechtenberg, and P. Gerlinger, "Rocket combustion chamber simulations using high-order methods," *Future Space-Transport-System Components under High Thermal and Mechanical Loads* (Springer, 2011), pp. 381–394.
- ⁵¹P. H. Joo, M. R. J. Charest, C. P. T. Groth, and Ö. L. Gülder, "Comparison of structures of laminar methane-oxygen and methane-air diffusion flames from atmospheric to 60 atm," *Combust. Flame* **160**(1), 1990–1998 (2013).
- ⁵²D. Martínez-Sanchis, A. Sternin, D. Sternin, O. Haidn, and M. Tajmar, "Analysis of periodic synthetic turbulence generation and development for direct numerical simulations applications," *Phys. Fluids* **33**, 125130 (2021).
- ⁵³M. L. Shur, P. R. Spalart, M. K. Strelets, and A. K. Travin, "Synthetic turbulence generators for RANS-LES interfaces in zonal simulations of aerodynamic and aeroacoustic problems," *Flow, Turbul. Combust.* **93**, 63–92 (2014).
- ⁵⁴R. H. Kraichnan, "Diffusion by a random velocity field," *Phys. Fluids* **13**, 22–31 (1970).
- ⁵⁵A. Sternin, N. Perakis, M. P. Celano, and O. Haidn, "CFD-analysis of the effect of a cooling film on flow and heat transfer characteristics in a GCH_4/GO_X rocket combustion chamber," in *Space Propulsion 2018*, Sevilla, 2018.
- ⁵⁶F. Zhang, H. Bonart, T. Zirwes, P. Habisreuther, and P. Bockhorn, "Direct numerical simulations of chemically reacting flows with the public domain code OpenFOAM," in *High Performance Computing in Science and Engineering '16* (Springer, 2015), vol. 14, pp. 221–236.
- ⁵⁷T. Zirwes, F. Zhang, J. Denev, P. Habisreuther, and H. Bockhorn, "Automated code generation for maximizing performance of detailed chemistry calculations in OpenFOAM," in *High Performance Computing in Science and Engineering '17* (Springer, 2018), pp. 189–204.
- ⁵⁸T. Zirwes, F. Zhang, J. A. Denev, P. Habisreuther, H. Bockhorn, and D. Trimis, "Improved vectorization for efficient chemistry computations in OpenFOAM for large scale combustion simulations," in *High Performance Computing in Science and Engineering '18* (Springer, 2019), pp. 209–224.
- ⁵⁹T. Zirwes, F. Zhang, P. Habisreuther, J. A. Denev, H. Bockhorn, and D. Trimis, "Implementation and validation of a computationally efficient DNS solver for reacting flows in OpenFOAM," in *14th World Congress on Computational Mechanics* (Scipedia, 2021).
- ⁶⁰H. Weller, G. Tabor, H. Jasak, and C. Fureby, "A tensorial approach to computational continuum mechanics using object-oriented techniques," *Comput. Phys.* **12**(6), 620–631 (1998).
- ⁶¹H. Weller, G. Tabor, H. Jasak, and C. Fureby, *OpenFOAM* (openCFD Ltd., 2017).
- ⁶²P. W. McDonald, "The computation of transonic flow through two-dimensional gas turbine cascades," *Proceedings of the ASME 1971 International Gas Turbine Conference and Products Show* (ASME, 1971).
- ⁶³R. W. MacCormack and A. J. Paullay, "Computational efficiency achieved by time splitting of finite difference operators," AIAA Paper No. 1972-154, 1972.
- ⁶⁴F. Zhang, T. Zirwes, H. Nawroth, P. Habisreuther, H. Bockhorn, and C. O. Paschereit, "Combustion-generated noise: An environment-related issue for future combustion systems," *Energy Technol.* **5**(5), 1045–1054 (2017).
- ⁶⁵F. Zhang, T. Zirwes, P. Habisreuther, and H. Bockhorn, "Effect of unsteady stretching on the flame local dynamics," *Combust. Flame* **175**, 170–179 (2017).
- ⁶⁶T. Zirwes, T. Häber, Z. Feichi, H. Kosaka, A. Dreizler, M. Steinhausen, C. Hasse, A. Stagni, D. Trimis, R. Suntz, and H. Bockhorn, "Numerical study of quenching distances for side-wall quenching using detailed diffusion and chemistry," *Flow, Turbul. Combust.* **106**, 649–679 (2021).
- ⁶⁷F. Zhang, T. Zirwes, T. Häber, H. Bockhorn, D. Trimis, and R. Suntz, "Near wall dynamics of premixed flames," in *Proceedings of the Combustion Institute*, 2020.
- ⁶⁸T. Zirwes, F. Zhang, P. Habisreuther, M. Hansinger, H. Bockhorn, M. Pfitzner, and D. Trimis, "Quasi-DNS dataset of a piloted flame with inhomogeneous inlet conditions," *Flow, Turbul. Combust.* **104**, 997–1027 (2020).
- ⁶⁹D. Goodwin, H. Moffat, and R. Speth (2017). "Cantera: An object-oriented software toolkit for chemical kinetics, thermodynamics and transport processes version 2.3.0b," Zenodo <https://doi.org/10.5281/zenodo.6387882>.
- ⁷⁰R. Kee, M. Coltrin, and P. Glarborg, *Chemically Reacting Flow: Theory and Practice* (Wiley, London, 2005).

- ⁷¹N. Slavinskaya, M. Abbasi, J. H. Starcke, and O. Haidn, "Methane skeletal mechanism for space propulsion applications," in Joint Propulsion Conference, Salt Lake City, 2016.
- ⁷²F. Winter, N. Perakis, and O. Haidn, "Emission imaging and CFD simulation of a coaxial single-element GO_x/GCH_4 rocket combustor," in Joint Propulsion Conference, Cincinnati, Ohio, 2018.
- ⁷³D. O. Lignell, J. H. Chen, and H. A. Schmutz, "Effects of Damköhler number on flame extinction and reignition in turbulent non-premixed flames using DNS," *Combust. Flame* **158**, 949–963 (2011).
- ⁷⁴B. Cuenot and T. Poinot, "Effects of curvature and unsteadiness in diffusion flames. Implications for turbulent diffusion combustion," in *Symposium (International) Combustion* (Elsevier, 1994), Vol. 25, 1383–1390.
- ⁷⁵N. Chakraborty, "Influence of thermal expansion on fluid dynamics of turbulent premixed combustion and its modelling implications," *Flow, Turbul. Combust.* **106**, 753–848 (2021).
- ⁷⁶D. Martínez-Sanchis, A. Sternin, K. Tagscherer, D. Sternin, O. J. Haidn, and M. Tajmar, "Interactions between flame topology and turbulent transport in high-pressure premixed combustion," *Flow, Turbul. Combust.* **109**(3), 4 (2022).
- ⁷⁷P. A. Durbin and B. A. Petersson-Reif, *Statistical Theory and Modelling of Turbulent Flows* (Wiley, Hoboken, 2001).
- ⁷⁸D. C. Wilcox, *Turbulence Modelling for CFD* (DCW, Canada, 2002).
- ⁷⁹S. Andrej, M.-S. Daniel, D. Sternin, O. Haidn, and M. Tajmar, "Characterisation and design of direct numerical simulations of turbulent statistically planar flames," *Aerospace* **9**, 530 (2022).